



Flow, turbulence, and drag associated with engineered log jams in a fixed-bed experimental channel

Sean J. Bennett ^{a,*}, S. Mohammad Ghaneeizad ^b, Michael S. Gallisdorfer ^a, Donghua Cai ^a, Joseph F. Atkinson ^b, Andrew Simon ^c, Eddy J. Langendoen ^d

^a Department of Geography, University at Buffalo, Buffalo, NY 14261-0055, USA

^b Department of Civil, Structural, and Environmental Engineering, University at Buffalo, Buffalo, NY 14260, USA

^c CardnoENTRIX, 1223 Jackson Avenue East, Suite 301, Oxford, MS 38655, USA

^d USDA-ARS National Sedimentation Laboratory, Oxford, MS 38655, USA

ARTICLE INFO

Article history:

Received 27 March 2015

Received in revised form 28 July 2015

Accepted 30 July 2015

Available online 4 August 2015

Keywords:

Engineered log jams

Drag force

Physical model

River restoration

ABSTRACT

Engineered log jams (ELJs) have become attractive alternatives for river restoration and bank stabilization programs. Yet the effects of ELJs on turbulent flow and the fluid forces acting on the ELJs are not well known, and such information could inform design criteria. In this study, a fixed-bed physical model was constructed to assess the introduction of ELJs along the Big Sioux River, SD. Two ELJ types were examined, referred to as ELJ-1 and ELJ-2. Both types were deflector jams, where ELJ-1 was rectangular and ELJ-2 was triangular, and oriented with one side attached to the channel bank. They were deployed either as single structures or in groups of two or three on the same side of the channel and at different separation distances. Results show that (1) time-mean and turbulent velocities and bed shear stresses were measurably altered near the ELJ, but spatially averaged flow just upstream and downstream of the structure was unaffected; (2) streamwise drag forces measured for the ELJs were significantly larger than the transverse forces, and the derived drag coefficients for the single structures were 2.72 ± 0.19 for ELJ-1 and 1.60 ± 0.37 for ELJ-2; and (3) the presence of an upstream structure created a near-bank wake region that extended a distance of more than 30 flow depths downstream, which greatly reduced drag forces and drag coefficients observed for the downstream structure by as much as 80%. These observations are further evidence of the efficacy of ELJs in providing near-structure scour pool development and bank protection downstream, and they can be used to inform and assess the design of ELJs for use in river restoration and bank stabilization projects.

© 2015 Elsevier B.V. All rights reserved.

1. Introduction

Natural accumulations of large wood (LW) are integral and beneficial components of many river systems worldwide. Geomorphically, LW can affect time-mean and turbulent velocities (Daniels and Rhoads, 2003); it can create patterns of localized erosion and deposition (Abbe and Montgomery, 1996; Buffington et al., 2002; Wallerstein and Thorne, 2004); and its placement has been linked to the development, spacing, and stability of pools (Montgomery et al., 1995). Ecologically, LW provides essential habitat and ecosystem services (Bisson et al., 1987; Lester and Boulton, 2008), it enhances hyporheic flow exchange (Lautz et al., 2006), and it can sequester nutrients and facilitate their processing in situ (Lester and Boulton, 2008; Flores et al., 2011). At relatively larger time and space scales, LW can positively influence the dynamic stability and integrity of fluvial landscapes (Collins et al., 2012).

For these reasons, engineered log jams (ELJs) have become attractive alternatives to conventional in-stream structures used for river

restoration and channel stability. For example, ELJs can be employed in river restoration projects for grade control and flow redirection (Abbe and Brooks, 2011). Abbe et al. (2003a) and Abbe et al. (2003b) showed that ELJs installed along the North Fork Stillaguamish River, WA, improved habitat indices, decreased bank erosion, and trapped additional wood in transit. Shields et al. (2004) described the design and installation of ELJs along Little Topashaw Creek, MS. While several structures failed because of a subsequent high-flow event and inadequate anchoring, the ELJs produced positive responses in fish communities (Shields et al., 2006). Brooks et al. (2004) reported on the installation of ELJs along the Williams River, NSW, AUS, which resulted in increased pool and riffle area and pool depth, increased sedimentation and channel complexity, and improved fish indices. Despite these successes, current design criteria for ELJs are sparse (see Shields et al., 2004; Brooks et al., 2006), and the morphodynamic responses of river corridors to the introduction of ELJs could be better predicted. The primary reasons for these perceived deficiencies may be attributed to (i) the relatively new technology and concept of ELJs, (ii) the lack of widespread deployment of ELJs by practitioners, and (iii) limited data on ELJ post-project assessment.

* Corresponding author.

E-mail address: seanb@buffalo.edu (S.J. Bennett).

Scaled models of river prototypes in laboratory channels can help fill these important gaps in the understanding of river morphodynamic responses to ELJs and to further develop and refine design criteria. Gallisdorfer et al. (2014) reviewed the basis for scaled physical models of ELJs and presented the necessary relations for analyzing the introduction of ELJs into the Big Sioux River, SD, USA, as an example application. The Big Sioux River is a relatively low sinuosity river with a very fine sand bed flowing across glacial outwash and alluvial sediments where the primary land use in the watershed is agriculture (row crops and pasture). The proposed installations of ELJs along this river are to reduce bank erosion and to decrease suspended sediment fluxes to downstream environments, which have adversely affected fish and aquatic life within the river (SDDENR, 2014). Using the 1.5-year recurrence interval flow rate, spatially averaged dimensions of the river channel, and characteristics for the available wood, Gallisdorfer et al. (2014) provided the scaling relations required to construct fixed- and movable-bed physical models and the design of two different ELJ structures. The focus of the current paper is to present experimental findings for the fixed-bed model where two types of ELJs were deployed alone and in groups of two or three of the same structure. The objectives are (i) to document the effects of ELJs on the time-mean and turbulent flow and boundary shear stress as compared to a channel without any structures present and (ii) to define the fluid forces acting on the structures, through direct and indirect means, using a variety of structure configurations. These experimental results should inform design criteria for ELJs in river restoration and bank stabilization programs.

2. Methodology

Following Gallisdorfer et al. (2014), dimensional analysis indicates that the primary scaling relationship for the model is the Froude number Fr , where the ratio (subscript r) between the field prototype (subscript p) and physical model (subscript m) is set to unity,

$$Fr_r = \frac{Fr_p}{Fr_m} = \frac{u_r}{\sqrt{g_r h_r}} = 1 \quad (1)$$

where u is time-averaged downstream flow velocity, g is gravitational acceleration, and h is average flow depth. To build the fixed-bed model, channel cross section data provided by the City of Sioux Falls were averaged to determine representative reach dimensions, and a flow frequency analysis of data collected near Dell Rapids, SD (USGS 0648100) defined the design discharge Q with a recurrence interval of 1.5 years ($Q_{1.5}$). Additional considerations for model construction included the following: (i) flow was fully turbulent, (ii) surface tension was ignored, (iii) the vertical scale was distorted relative to the horizontal scale, (iv) dimensions of the available wood to be employed in the ELJs, as provided by the City of Sioux Falls, and (v) dimensions of the experimental apparatus (Wallerstein et al., 2001; Gallisdorfer et al., 2014). Given these data and qualifications, Table 1 summarizes the dimensions of the field prototype and the fixed-bed physical model (see Gallisdorfer et al. (2014) for additional details).

Table 1
Summary of prototype (Big Sioux River, SD) and model dimensions.

Parameter	Prototype	Model
Discharge Q ($\text{m}^3 \text{s}^{-1}$)	51.1	0.0268
Top width (m)	40.5	1.9
Bottom width B (m)	40.5	1.9
Depth h (m)	2.2	0.114
Velocity u (m s^{-1})	0.574	0.128
Bed slope S_B	0.00047	0.0005 ^a
Bed texture (mm)	0.08 to 0.1	NA
Froude number Fr	0.124	0.124
Reynolds number Re	10^6	10^4

^a Later corrected to 0.00005, based on bed shear stress calculations.

The experiments were conducted in a tilting, recirculating (open loop) flume, 1.9 m wide, 7 m long, and 0.5 m deep with 90° fixed banks (Fig. 1). Three sump pumps were operated in parallel to deliver a maximum discharge of 0.0268 m^3/s , monitored using an in-line flow meter, and this discharge corresponds to the 1.48-year return period within the prototype (which is close to the target design discharge of $Q_{1.5}$; Gallisdorfer et al., 2014). The 6-inch inflow pipe was buried into a 2.0-m-wide, 0.9-m-deep, and 0.9-m-tall headbox filled with cobbles, which dissipated all pump-related turbulence. Fifteen flow straighteners, 0.20 m tall and 0.37 m deep, were installed evenly across the entrance to the flume and downstream of the headbox, and ten adjustable vertical vanes 0.16 m wide and 0.26 m tall were installed at the flume exit to regulate flow depth within the flume. Vertical profiles of velocity and at-a-point depth measurements along and across the test section of the flume confirmed uniform flow conditions (described below). Flume slope was adjusted manually and checked using a rod and level (elevation resolution is ± 1 mm).

Two ELJ structures were employed, referred to as ELJ-1 and ELJ-2 (Fig. 2). These structures are slightly modified versions of a bank-attached deflector jam commonly used in field applications (Brooks et al., 2006). These ELJ types were chosen to examine the effect of structure shape and penetration distance on the flow field and drag forces. Element dimensions used in the ELJs were scaled based on the width ratio of prototype-to-flume and available wood (Gallisdorfer et al., 2014). Each structure included five layers of wooden elements: three layers of key elements with a diameter of 0.032 m; and two layers of notched, cross-spanning elements with an effective diameter of 0.019 m. All elements exposed to the flow (upstream and cross-stream) had simulated wooden root wads attached: disks 0.063 m in diameter and 0.014 m thick. Penetration distances into the flow were 0.40 m (0.21 B) for ELJ-1 and 0.28 m (0.15 B) for ELJ-2, corresponding to respective values of 8.5 and 6.1 m for the prototype. The differences between these two structures are overall size and orientation and the penetration distance into the flow. In the field, such ELJ structures would be fixed in place (immobile) and ballasted or backfilled with gravel and cobbles (Brooks et al., 2006).

Downstream (drag) and cross-stream (transverse) forces acting on a single ELJ were measured at 240 Hz by a Futek MBA400 biaxial load cell, which has a dynamic range of 230 N and a resolution of 0.03 N. This load cell was carefully calibrated in situ using fully saturated and submerged ELJs and a precise force scale with a range of 0 to 5 N. Forces were measured for the entire structure, given that all members were interconnected and fixed in place; and the ELJ was mounted to the load cell at a single location (Fig. 2E). The instrumented ELJ was suspended pendant to flow with about a 2-mm gap between the bed and wall of the flume. All forces reported here are based on 180-s time averages.

Experiments considered both single- and multiple-structure installations. Fifteen different configurations were examined, each employing a specific number of structures and collecting specific data. For each configuration using more than one ELJ, one or more experimental runs were conducted in which ELJ spacing was varied. For all runs with an ELJ, an instrumented structure was deployed at a fixed location 4.6 m downstream of the headbox. One or two additional ELJ structures of the same type would be installed either upstream or downstream of the instrumented structure on the same side of the channel. Center-to-center spacing between these structures is reported. Table 2 summarizes each configuration and the data collected.

Flow velocities were collected using a side-looking Nortek Vectrino II acoustic Doppler velocimeter (ADV). Vertical profiles of fluctuating velocities in the downstream u (x -direction; positive in the downstream direction), vertical v (y -direction; positive upward), and cross-stream w (z -direction; positive toward the left bank looking downstream). Velocity data were collected across the entire cross section and in the near-field surrounding the ELJ. For the cross sections, data were obtained in 24 vertical profiles spaced 0.05 to 0.1 m across the flume, and each profile contained 11 sampling locations spaced at intervals of 0.01 to 0.02 m

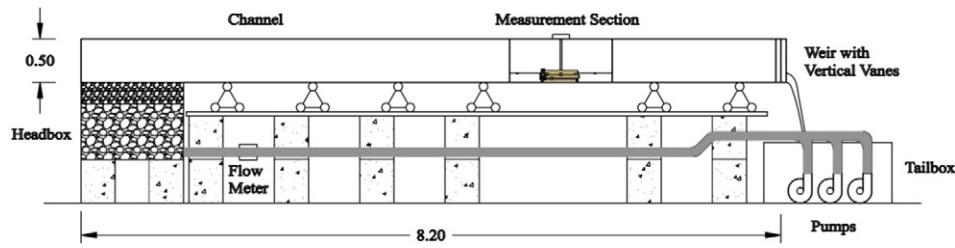


Fig. 1. Schematic diagram of the experimental channel (Gallisdorfer et al., 2014). Three sump pumps in the tailbox are connected to a single discharge pipe and provide flow in the main channel (flow is left to right). Flow rate is monitored with an in-line meter. The headbox is filled with cobbles to help dampen pump-related turbulence, and a downstream weir composed on vertical vanes controls flow depth. The measurement section shows an ELJ structure mounted to the biaxial load cell secured to the cart on the flume rails. All dimensions are in meters.

(Fig. 3A). Higher spatial resolutions were employed near the ELJ. In the presence of a single ELJ, two cross sections were selected for measurement: $0.83 h$ (0.095 m) upstream and downstream of the structure. When multiple structures were present, velocity data were collected upstream and downstream of the instrumented structure at a distance of $2 h$ (0.228 m). This procedure included eight vertical profiles spaced at 0.05 m from the sidewall, and each profile contained five vertical locations spaced at intervals of 0.015 to 0.02 m (Fig. 3B). At all sampling locations, velocities were recorded for 120 s at 75 Hz . When processing, all data with correlations < 0.7 were rejected (WinADV; Lane et al., 1998; Wahl, 2000), and all erroneous spikes were removed (phase-space threshold method; Goring and Nikora, 2002). These methods typically deleted about 4% of the observations.

The ADV data were processed to derive time- and space-averaged velocity and turbulence parameters as well as determinations of bed shear stress. To define spatially averaged flow and turbulence parameters, all data were first time-averaged at-a-point. Second, all flow parameters were spatially averaged vertically and horizontally. For u , v , and w flow velocities, a no-slip condition was assumed along the walls (at $y/h = 0$ and $z/B = 0, 1$), and the velocity at the water surface ($y/h = 1$) was assumed to be equal to the measured value just below it ($y/h = 0.78$). Using downstream flow velocity u as an example, spatially-averaged velocity $\langle u \rangle$ is defined as

$$\langle u \rangle = \frac{1}{B} \frac{1}{h} \int_0^B \int_0^h \bar{u}(z, y) dz dy \quad (2)$$

where $\bar{u}(z, y)$ is the time-averaged value at-a-point. The spatially-averaged downstream flow velocity for the reference condition, denoted as u_0 , is used to normalize all velocity and turbulence data. For turbulence and kinetic energy parameters defined below, the values at the bed ($y/h = 0$) were assumed to be equal to the nearest-bed value ($y/h = 0.11$), whereas values at the sidewall and water surface ($y/h = 1$ and $z/B = 0, 1$) were assumed to be zero. Spatially-averaged velocity magnitude U_{mag} is defined as

$$U_{mag} = \sqrt{\langle u \rangle^2 + \langle v \rangle^2 + \langle w \rangle^2}. \quad (3)$$

Root-mean-square (denoted by subscript *rms*) of each velocity component and turbulent kinetic energy k are defined as

$$u_{rms} = \sqrt{\overline{u'^2}}; v_{rms} = \sqrt{\overline{v'^2}}; w_{rms} = \sqrt{\overline{w'^2}}; k = \frac{1}{2} (\overline{u'^2} + \overline{v'^2} + \overline{w'^2}) \quad (4)$$

where $u' = u - \bar{u}$, $v' = v - \bar{v}$, and $w' = w - \bar{w}$.

For wide open-channel flows with $B/h > 6$, boundary shear stress τ_{hs} can be defined as a function of flow depth h (or hydraulic radius) and energy (or bed) slope S ,

$$\tau_{hs} = \rho g h S \quad (5)$$

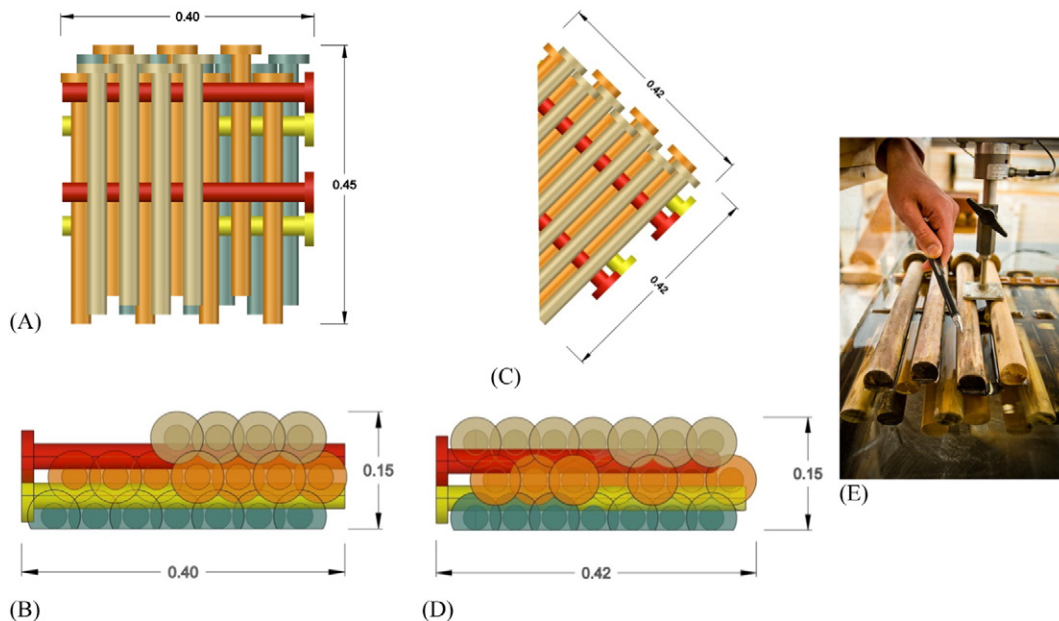


Fig. 2. Model drawings of showing plan and frontal views of ELJ-1 (A, B) and ELJ-2 (C, D), with dimensions in meters (Gallisdorfer et al., 2014). For the ELJs, flow would move from top to bottom with the near stream bank to the left. (E) Photograph of ELJ-1 mounted to the biaxial load cell looking upstream (photograph by D. Levere).

Table 2

Summary of experimental configurations (15 in total) and the data collected; individual runs (39 in total) for each configuration are identified by variations in spacing between structures (all structures were deployed on the same side of the channel).

Configuration	ELJ type	No. of structures	Spacing between structures	Instrumented structure	Data collected ^a		
					Cross-sectional flow	Near-field flow	Force
1	NA	0	–	–	X	–	–
2	1	1	–	–	X	X	X
3	1	2	7.5 h, 15 h, 30 h	Downstream	–	X	X
4	1	2	5 h, 10 h, 12.5 h, 17.5 h, 20 h, 22.5 h, 25 h, 27.5 h	Downstream	–	–	X
5	1	3	5 h	Upstream	–	–	X
6	1	3	5 h	Center	–	–	X
7	1	3	5 h	Downstream	–	–	X
8	1	3	7.5 h, 10 h, 12.5 h, 15 h	Downstream	–	–	X
9	2	1	–	–	X	X	X
10	2	2	7.5 h, 15 h, 30 h	Downstream	–	X	X
11	2	2	5 h, 10 h, 12.5 h, 17.5 h, 20 h, 22.5 h, 25 h, 27.5 h	Downstream	–	–	X
12	2	3	5 h	Upstream	–	–	X
13	2	3	5 h	Center	–	–	X
14	2	3	5 h	Downstream	–	–	X
15	2	3	7.5 h, 10 h, 12.5 h, 15 h	Downstream	–	–	X

^a Cross-sectional flow refers to velocity measurements obtained upstream and downstream of the ELJ across the entire flume width. Near-field flow refers to velocity measurements obtained upstream and downstream of the ELJ but limited in distance across the flume to the penetration width of the structure. Force refers to drag and transverse forces measured on the instrumented ELJ.

where ρ is fluid density. The distribution of downstream flow velocity is described by the Kármán–Prandtl ‘law of the wall’ in the near-bed region (usually $y < 0.2h$), defined as

$$\frac{u}{u_*} = \frac{1}{\kappa} \ln \left(\frac{y}{y_0} \right); \tau_u = \rho u_*^2 \quad (6)$$

where τ_u and u_* are bed shear stress and shear velocity, respectively, κ is von Kármán’s coefficient (0.41), and y_0 is the zero-velocity roughness height. Assuming linear variations with height above the bed for Reynolds stress and turbulent kinetic energy k , these measurements can be extrapolated to determine bed stress values (τ_R based on Reynolds stress and τ_k based on turbulent kinetic energy),

$$\tau_R = -\rho \overline{u'v'}|_{y=0}; \tau_k = ck|_{y=0} \quad (7)$$

where c varies from 0.18 to 0.21 (Soulsby, 1983; Williams et al., 1999; Huthnance et al., 2002).

Drag coefficients of the ELJs can be determined from the force measurements. The drag coefficient C_D is defined as

$$C_D = \frac{2F_D}{\rho U^2 A} \quad (8)$$

where U is a characteristic velocity, A is the area of the ELJ exposed to the flow, and F_D is drag force measured directly from the load cell.

3. Results

The objectives of the experiments were to document the effects of ELJs on the time-mean and turbulent flow and boundary shear stress as compared to a channel without any structures present and to define the fluid forces acting on select structures. As summarized in Table 2, 15 experimental configurations comprising 39 individual runs were conducted. The experimental results are presented in four groups: spatial patterns of (i) time-averaged cross-sectional flow and (ii) bed shear stress for a single ELJ structure, (iii) spatial patterns of time-averaged near-field flow for one or two ELJ structures, and (iv) fluid forces acting on ELJs. From these experimental observations, an analysis of the fluid momentum within the experimental domain is discussed, and a critical assessment of the drag coefficients of the ELJs is presented. Much of the data are compared to the reference condition, in which no ELJ was present. Table 3 summarizes the spatially-averaged values for velocity, turbulence, and shear stress parameters for the reference condition and for cross-sections upstream and downstream of a single ELJ structure. The derivation and significance of these parameters are presented below.

3.1. Spatial patterns of time-averaged cross-sectional flow for a single ELJ structure

Select velocity and turbulence parameters for channel cross-sections were time-averaged at-a-point, normalized by u_0 and u_0^2 and plotted as contour maps in Figs. 4 to 8. In these figures, the reference condition is used as a basis for comparison of the cross-sectional flow data results obtained immediately upstream and downstream of the ELJ structures.

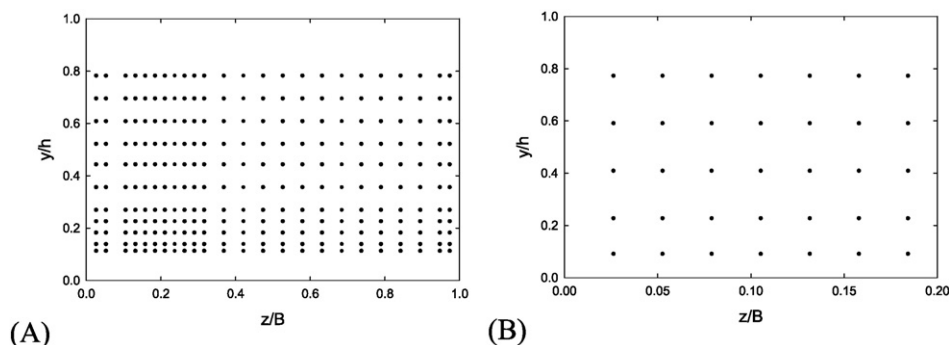


Fig. 3. Locations of velocity measurements obtained for the (A) entire cross section and (B) near-field.

Table 3

Summary of spatially averaged flow values for select cross sections (using Table 2, the reference condition is configuration 1, ELJ-1 is configuration 2, and ELJ-2 is configuration 9).

	d (m)	$\langle u \rangle$ (m s ⁻¹)	$\langle v \rangle$ (m s ⁻¹)	$\langle w \rangle$ (m s ⁻¹)	$\langle U_{mag} \rangle$ (m s ⁻¹)	$\langle u_{rms} \rangle$ (m s ⁻¹)	$\langle v_{rms} \rangle$ (m s ⁻¹)	$\langle w_{rms} \rangle$ (m s ⁻¹)	$\langle k \rangle$ (10 ⁻⁴ m ² s ⁻²)	$\langle \tau_u \rangle$ (Pa)	$\langle \tau_v \rangle$ (Pa)	$\langle \tau_w \rangle$ (Pa)
Reference condition ^a	0.114	0.117	0.010	-0.004	0.117	0.009	0.010	0.006	1.26	0.051	0.059	0.065
ELJ-1 US	0.115	0.117	0.009	0.016	0.119	0.010	0.011	0.006	1.35	0.063	0.062	0.074
ELJ-1 DS	0.115	0.116	0.008	0.005	0.118	0.011	0.011	0.007	1.93	0.057	0.089	0.115
ELJ-2 US	0.114	0.118	0.009	0.008	0.119	0.009	0.011	0.006	1.32	0.064	0.060	0.071
ELJ-2 DS	0.112	0.119	0.010	0.005	0.119	0.010	0.011	0.006	1.50	0.033	0.064	0.081

^a US, DS refers to upstream or downstream of the ELJ.

The cross-sectional flow distribution for the reference condition is consistent with smooth-walled, rectangular, open channel flows (e.g., Nezu and Nakagawa, 1993). The downstream velocity component u/u_0 exhibits a parabolically shaped distribution of values in space, and the spatially-averaged vertical $\langle v \rangle$ and cross-stream $\langle w \rangle$ velocity components are relatively small in comparison: $\langle u \rangle \approx 12\langle v \rangle \approx 30\langle w \rangle$ (Table 3). Contour maps also display the spatial distributions of u_{rms}/u_0 (Fig. 5), v_{rms}/u_0 (Fig. 6), w_{rms}/u_0 (Fig. 7), and k/u_0^2 (Fig. 8). Maxima for these turbulence parameters occur at the flume bed along the flow centerline, and minima occur along the flume walls and near the water surface. For the spatially-averaged values, $\langle u_{rms} \rangle \approx \langle v_{rms} \rangle \approx 1.5\langle w_{rms} \rangle$ (Table 3). These ratios are slightly different to observations in field studies that suggested $\langle u_{rms} \rangle$ is the dominant contributor to turbulence (Sukhodolov et al., 1998; Kim et al., 2000; Daniels and Rhoads, 2003). This minor turbulence anisotropy likely would cause secondary flow circulation (e.g., Nezu and Nakagawa, 1993), but this effect was not investigated.

The presence of ELJs has varying effects on the distributions and magnitudes of velocity and turbulence. Upstream of the ELJs, magnitudes are slightly diminished near the structure and slightly enhanced away from the structure within the main channel flow (Fig. 4). Flow is more strongly decelerated near the inner bank just downstream of the structures where some flow recirculation is observed, whereas flow is accelerated in the main channel away from the structures. This is to be expected because the structure is designed to be nonporous, with little to no through-flow (Gippel et al., 1996; Brooks et al., 2006; Manners et al., 2007). This effect can be achieved by employing a relatively high vegetation density (Bennett et al., 2008). In both experiments, a pronounced, vertically oriented shear layer forms downstream of the ELJ,

as demarcated by vertically oriented isovels (Fig. 4). The spatial extent of the shear layer in the transverse direction is comparable in magnitude to the penetration distance of the ELJ. The normalized velocity differential across the shear layer observed for ELJ-1 is larger than that observed for ELJ-2. Contour maps for v/u_0 and w/u_0 show some altered magnitudes and directions of flow within the shear layers, but these velocities are only about 10% of the magnitude observed for u/u_0 (reported in Cai, 2014). The locations of the upstream measurements clearly are within the flow field affected by the ELJs, in agreement with previous observations (Brooks et al., 2006; Svoboda and Russell, 2011).

The ELJs also affected turbulence parameters. Upstream of the ELJs, there is little to no observable change in the magnitude or distribution of the turbulent velocities (Figs. 5 to 7) and kinetic energy (Fig. 8) as compared to the reference condition. Yet these same parameters are significantly altered downstream of the structures. In each case, turbulence intensities and turbulent kinetic energy are increased along the shear layer, by as much as a factor of five when compared to the reference conditions. Moreover, the area of high turbulence intensity extends from the bed to the water surface, which coincides in space with the location of the shear layer, and the loci of all turbulence maxima occur along this shear layer rather than at the bed, as in the case for flow upstream of the structure and for flow in the reference condition. These increases in turbulence intensity are greater downstream of ELJ-1 as compared to ELJ-2. In contrast, turbulent velocities and kinetic energy are reduced in the near-bank region downstream of the ELJs by as much as a factor of three, thus providing further evidence for the efficacy of ELJs as bank protection installations (Daniels and Rhoads, 2003; Abbe et al., 2003b). The presence of ELJs does not produce any variation in the spatially-averaged flow, as can be seen with values of velocity

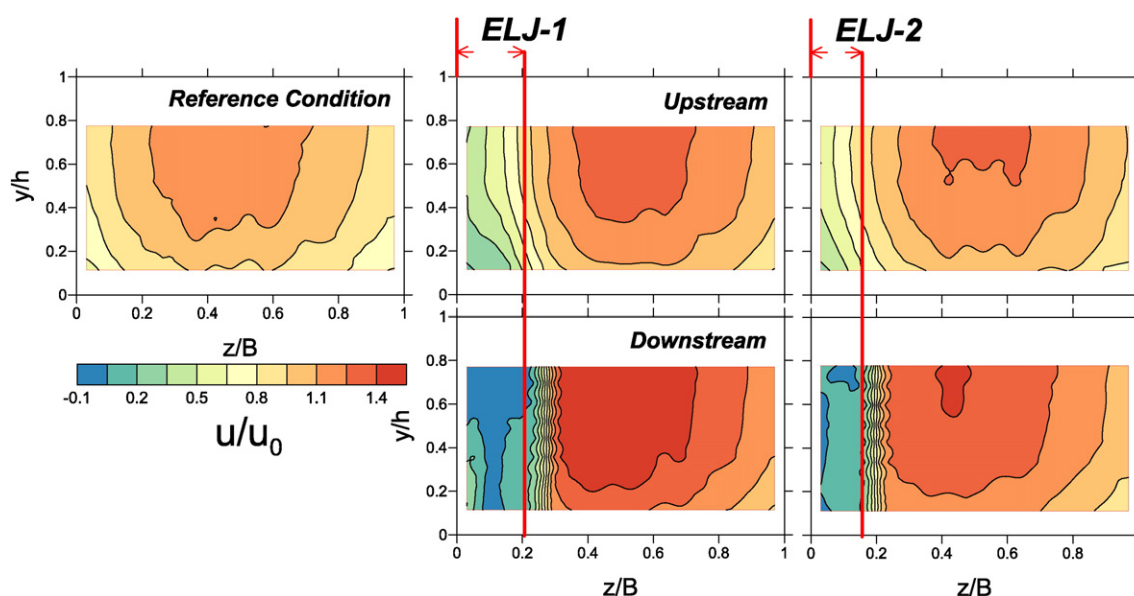


Fig. 4. Contour plots of normalized time-averaged downstream velocity. The reference condition map (on left) shows the flow field without any structures present (configuration 1). The additional maps show ELJ-1 (middle; configuration 2) and ELJ-2 (right; configuration 9) for the upstream (upper) and downstream (lower) cross sections. The penetration distances of the ELJs into the flow also are shown as vertical lines.

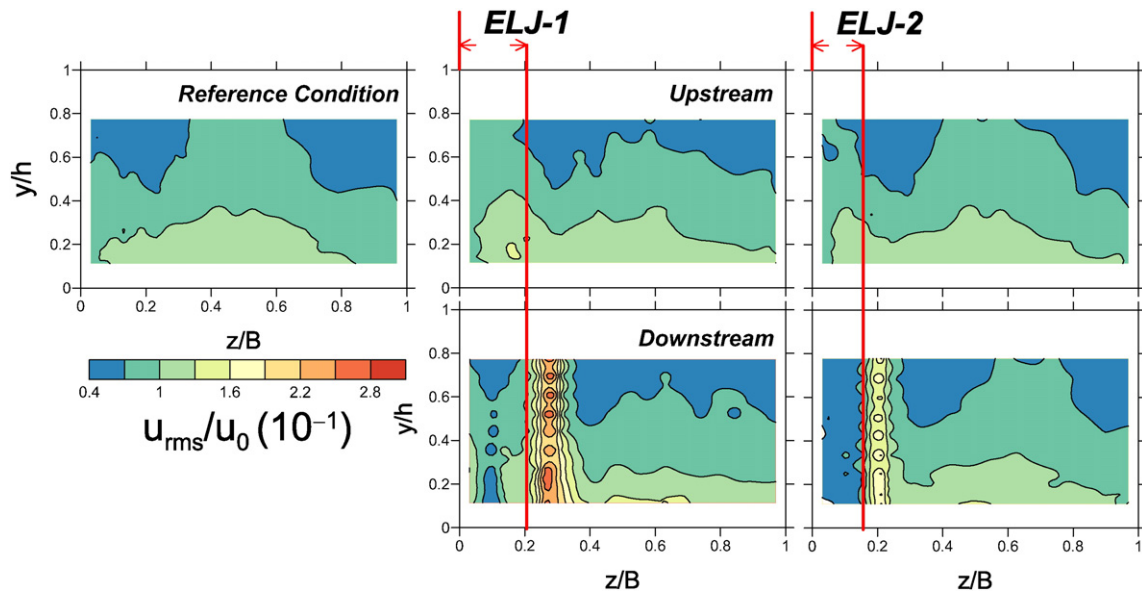


Fig. 5. Contour plots of normalized time-averaged u_{rms} velocity. Refer to Fig. 4 for additional details.

magnitude U_{mag} in Table 3. The results are similar to field observation on how LW affects flow, where the LW creates a zone of high turbulence energy near the LW-main flow interface and a near-bank zone of dampened velocities downstream of the LW (Daniels and Rhoads, 2003; Manners et al., 2007).

3.2. Spatial patterns of bed shear stress for a single ELJ structure

Approaches to quantify boundary shear stress include application of the conservation of fluid momentum (Eq. (5)), analysis of near-bed gradients in downstream flow velocity (Eq. (6)), and an examination of the distributions of Reynolds stresses and turbulent kinetic energy (Eq. (7)). For steady, uniform, clear-water, turbulent open-channel flows over flat beds, these approaches theoretically should converge to a single value, within experimental error (Nezu and Nakagawa, 1993; Bennett et al., 1998; Biron et al., 2004). That is, $\tau_{hs} \approx \tau_u \approx \tau_R \approx \tau_k$ should be observed for the reference condition.

These bed shear stress determinations show that τ_R and τ_k are consistent with each other for the reference condition with distance across the flume (Fig. 9). Although much more variable, τ_u also shows a similar variation, where all three estimates exhibit maxima near the center of the channel, decreasing toward the flume sidewalls. Each estimate can be spatially-averaged, giving $\langle \tau_u \rangle = 0.051$ Pa, $\langle \tau_R \rangle = 0.065$ Pa, $\langle \tau_k \rangle = 0.059$ Pa. Referring to Eq. (7), a value of $c = 0.23$ is found here, which is just slightly larger than the range previously reported. In contrast, $\tau_{hs} = 0.56$ Pa using the values in Table 1. As previously noted, elevation resolution for the flume bed slope was ± 1 mm. For $S = 0.0005$, this is a drop in elevation of 3.5 mm over the 7-m flume length. As such, a measurement error in this bed slope determination is likely, which could explain the relatively higher value found for τ_{hs} . Based on these results, $\langle \tau_u \rangle \approx \langle \tau_R \rangle \approx \langle \tau_k \rangle$, and a mean boundary shear stress, τ_0 can be defined by $\langle \tau_k \rangle$, or $\tau_0 = 0.059$ Pa. For open-channel flows with complex geometries, such as in the presence of engineered log jams, bed shear stress determined by $\langle \tau_k \rangle$ may be superior to other methods (Biron et al., 2004). Using $\tau_0 = \tau_{hs}$ in Eq. (5) gives $S = 0.00005$, which is a very

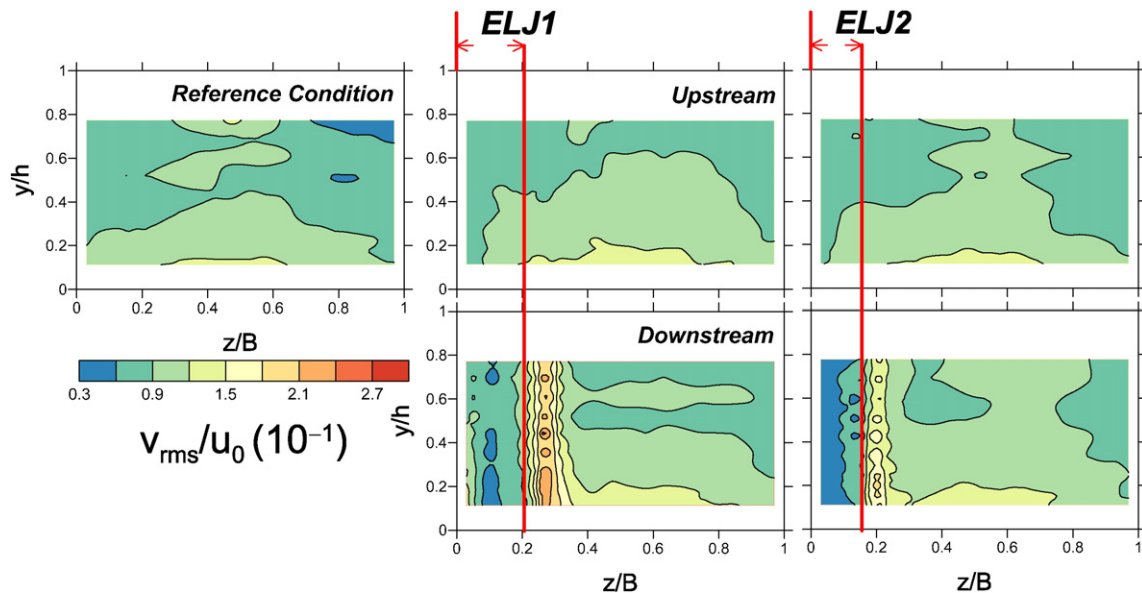


Fig. 6. Contour plots of normalized time-averaged v_{rms} velocity. Refer to Fig. 4 for additional details.

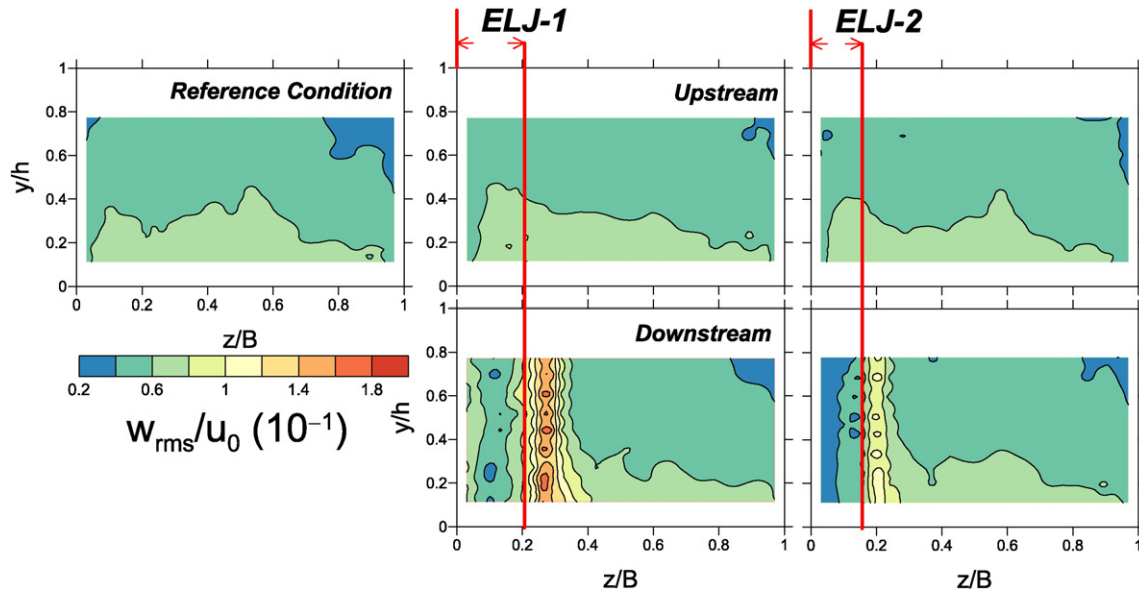


Fig. 7. Contour plots of normalized time-averaged w_{rms} velocity. Refer to Fig. 4 for additional details.

small slope to accompany these modest boundary shear stresses. This corrected value of bed slope is used hereafter.

Upstream of the ELJs, values of bed shear stress across the channel do not deviate significantly from the reference condition (Fig. 9). Downstream of the ELJs, bed shear stress is strongly affected. In the near-bank regions downstream of the ELJs, τ_R and τ_k are greatly suppressed (by a factor of two) compared to the reference condition. Bed shear stresses are greatly enhanced (by as much as a factor of eight) just outside the penetration distance, coinciding with the shear layer. Based on these distributions, the greatest potential for erosion and pool development on the stream bed is just outside of the ELJ penetration distance as previously suggested (Buffington et al., 2002; Wallerstein and Thorne, 2004).

3.3. Spatial patterns of near-field flow for one or two ELJ structures

Additional flow and turbulence data were collected just upstream and downstream of a structure in the presence of two structures. For

illustrative purposes, Fig. 10 shows the normalized downstream flow velocity; and Fig. 11 shows the normalized turbulent kinetic energy for the reference condition, in the presence of one structure, and in the presence of two structures with varying spacing. In the latter case, flow data were collected for the downstream structure.

In the upstream areas, flow is similar to the reference condition, with some backwater regions observable near the bed, especially near the bank (Fig. 10). The downstream areas show decelerated and less turbulent flow in regions protected by the ELJ, and accelerated flow and higher turbulence values along the mixing layer at the interface between the structure and the main flow.

When a second structure is present upstream, the near-field velocity metrics show evidence of skimming flow and wake interaction. When the structure spacing is $< 7.5 h$, the near-field values of u/u_0 and k/u_0^2 display reduced magnitudes, especially in the near-bank regions upstream of the structure and in the regions downstream of the structure (Figs. 10 and 11). Increasing this spacing, however, creates transverse gradients of flow velocity and turbulent kinetic energy, where contour lines for

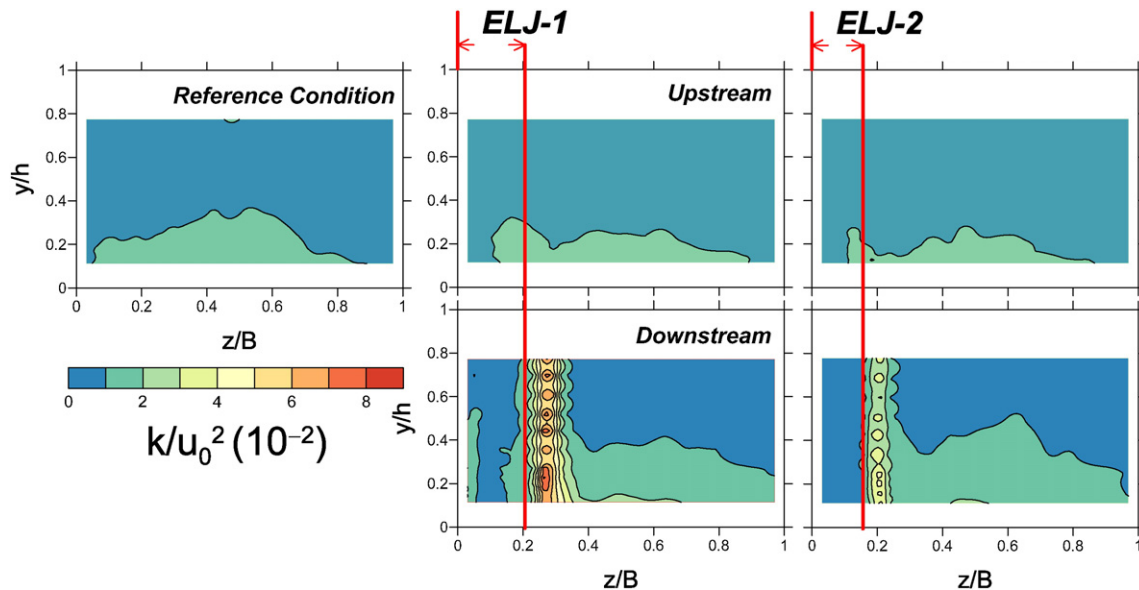


Fig. 8. Contour plots of normalized time-averaged turbulent kinetic energy k . Refer to Fig. 4 for additional details.

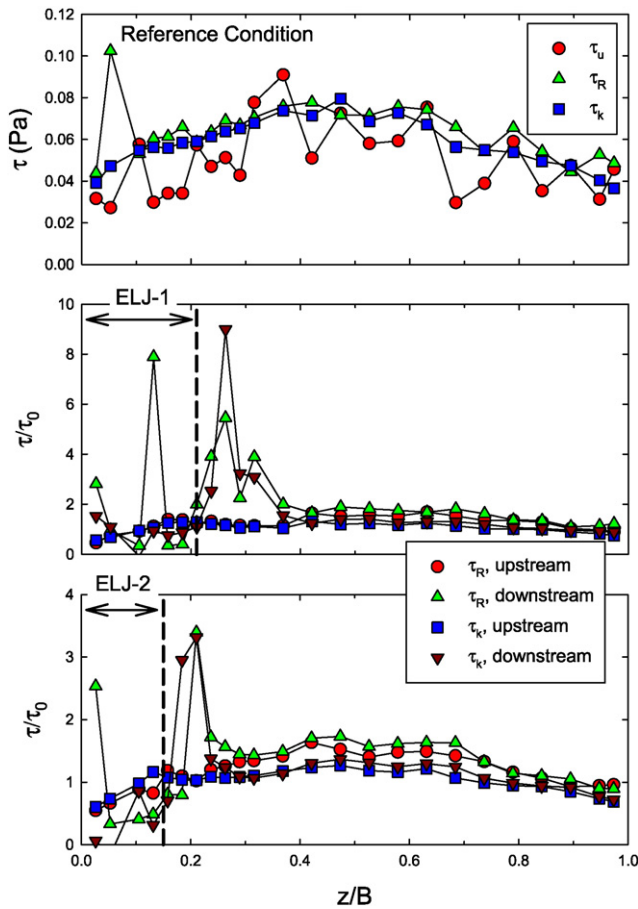


Fig. 9. Transverse distributions of bed shear stress in the reference condition (upper plot; configuration 1) and just upstream and downstream of ELJ-1 (middle plot; configuration 2) and ELJ-2 (lower plot; configuration 9) using different techniques. For the reference condition plot, bed shear stress values are dimensional; whereas for the ELJ plots, bed shear stress is normalized by the mean boundary shear stress. The penetration distance of the ELJs into the flow also is shown.

u/u_0 and k/u_0^2 become vertically oriented. Although the near-bank regions display relatively low flow velocities and turbulent kinetic energy values for structure spacing up to 15 h , more complex hydrodynamic interactions are observable at the largest structure spacing. At 30 h , turbulence values are enhanced upstream and downstream of the structures.

To quantify the downstream effects of this structure-induced wake, spatially-averaged downstream flow velocity and turbulent kinetic energy can be defined for the incident flow velocity of the downstream structure when two structures are deployed. These variables are defined as $\langle u_n \rangle$ and $\langle k_n \rangle$, respectively, employing Eq. (2) where the limits of the integration are restricted to the near-field data (Figs. 3b, 10, and 11). These values are then normalized by the equivalent values observed upstream of the single structure deployment, thereby defining $V^* = \langle u_n \rangle / \langle u_{n0} \rangle$ and $K^* = \langle k_n \rangle / \langle k_{n0} \rangle$. For both structures, the reduction of the normalized downstream flow velocity V^* is pronounced in magnitude and extensive in space, achieving reductions of about 80% at separation distances of 30 h downstream (Fig. 12). Yet the normalized turbulence kinetic energy K^* follows a different pattern. At a relatively small separation distance of 7.5 h , K^* values are reduced by about 50% for both structures (Fig. 12). At a distance of 15 h , no reductions in K^* are observed; whereas at a distance of 30 h , values of K^* increase to about 200%. This observation suggests that the wake region for both structures extends beyond 30 h based on the downstream velocity component (Figs. 10 and 12). In addition, the turbulent wakes created by the upstream structure and its associated shear layer actively interact with the near-field of the downstream structure when separation distances exceed 15 h (Figs. 11 and 12). These interactions could include flow

reattachment of the upstream eddies or the penetration of turbulent eddies shed from the upstream structure, which may be important considerations for the installation of successive ELJs in the prototype.

3.4. Fluid forces acting on ELJs

Forces were measured on a single ELJ in the downstream (drag force F_D , positive in the downstream direction) and transverse (cross-stream force F_T , positive toward the left or opposite bank looking downstream) directions. For a single structure placed in the flow, $F_D = 0.851 \pm 0.060$ N and $F_T = -0.023 \pm 0.089$ N for ELJ-1, and $F_D = 0.352 \pm 0.080$ N and $F_T = 0.007 \pm 0.088$ N for ELJ-2. The transverse force F_T is not discussed further because it was small ($F_D \gg F_T$) and did not change appreciably in any of the experimental configurations. Figs. 13 and 14 summarize the drag force measurements, where the error bars represent the standard deviation of each measurement period. The drag force measured for ELJ-1 is about 2.4 times larger than that measured for ELJ-2, and this can be attributed to differences in the size, shape, and penetration distance of the structures. For comparison, these values of F_D are similar in magnitude to the laboratory measurements of Gippel et al. (1996) and Wallerstein et al. (2002), but lower than Turcotte et al. (2015).

The measured drag forces on ELJs are reduced significantly by the presence of structures placed upstream. Fig. 13 shows that, in general, $F_D \approx 0.3 \pm 0.07$ N, or $F_D/F_{D0} \approx 0.3 \pm 0.08$, for ELJ-1 when another structure is present upstream, where F_{D0} is the drag force measured for the single structure, and this reduction does not vary with the spacing of structures up to 30 h . Fig. 14 shows that, in general, $F_D \approx 0.05$ to 0.15 ± 0.067 N, or $F_D/F_{D0} \approx 0.10$ to 0.30 ± 0.19 , for ELJ-2 when another structure is present upstream. In contrast to ELJ-1, the reduced drag force acting on ELJ-2 increases once $x/h \geq 15$ when two structures are present, and it increases once $x/h \geq 7.5$ when three structures are present. The trends are not statistically significant given the error bars of the measurements. These results suggest that the region of flow deceleration (the wake region) noted earlier causes reduced F_D values of a similar magnitude ($\sim 80\%$). Force measurements obtained for the middle structure within a three-structure sequence are no different than those observed for the downstream structure for equivalent spacing (Figs. 13 and 14). Moreover, force measurements obtained for the upstream structure within a three-structure sequence spaced at 5 h are nearly identical to those obtained for a single structure.

3.5. Drag coefficients for ELJs

Values of the drag coefficient C_D for ELJs can be determined from the force measurements using Eq. (8), and several options exist to define the characteristic velocity U . The spatially-averaged flow velocity for the entire cross-section with no ELJ present flow velocities is used here (the reference condition, Table 2), given that this parameter typically would be available for design purposes.

Drag coefficients for the single ELJs and corresponding velocity values are summarized as follows: $C_D = 2.72 \pm 0.19$ for ELJ-1, and $C_D = 1.60 \pm 0.37$ for ELJ-2 (Fig. 15). The drag coefficient for ELJ-1 is higher than that observed for ELJ-2 because of its size, shape, and orientation. The uncertainty range observed for the force measurements is assumed to be higher than the uncertainty of the spatially-averaged flow velocity, and this latter uncertainty is ignored in the reported values.

Drag coefficients are significantly reduced when additional ELJ structures are present upstream. Fig. 15 shows the reduction in C_D when ELJs are placed upstream of the instrumented structure. For ELJ-1, C_D decreases from about 2.72 ± 0.19 to about 0.88 ± 0.24 (a reduction of about 68%). For ELJ-2, C_D decreases from about 1.60 ± 0.37 to about 0.27 ± 0.31 (a reduction of about 83%). In both cases, these reductions in the drag coefficient are maintained even as spacing between the structures increases (up to $x/h = 30$). The drag coefficients for both

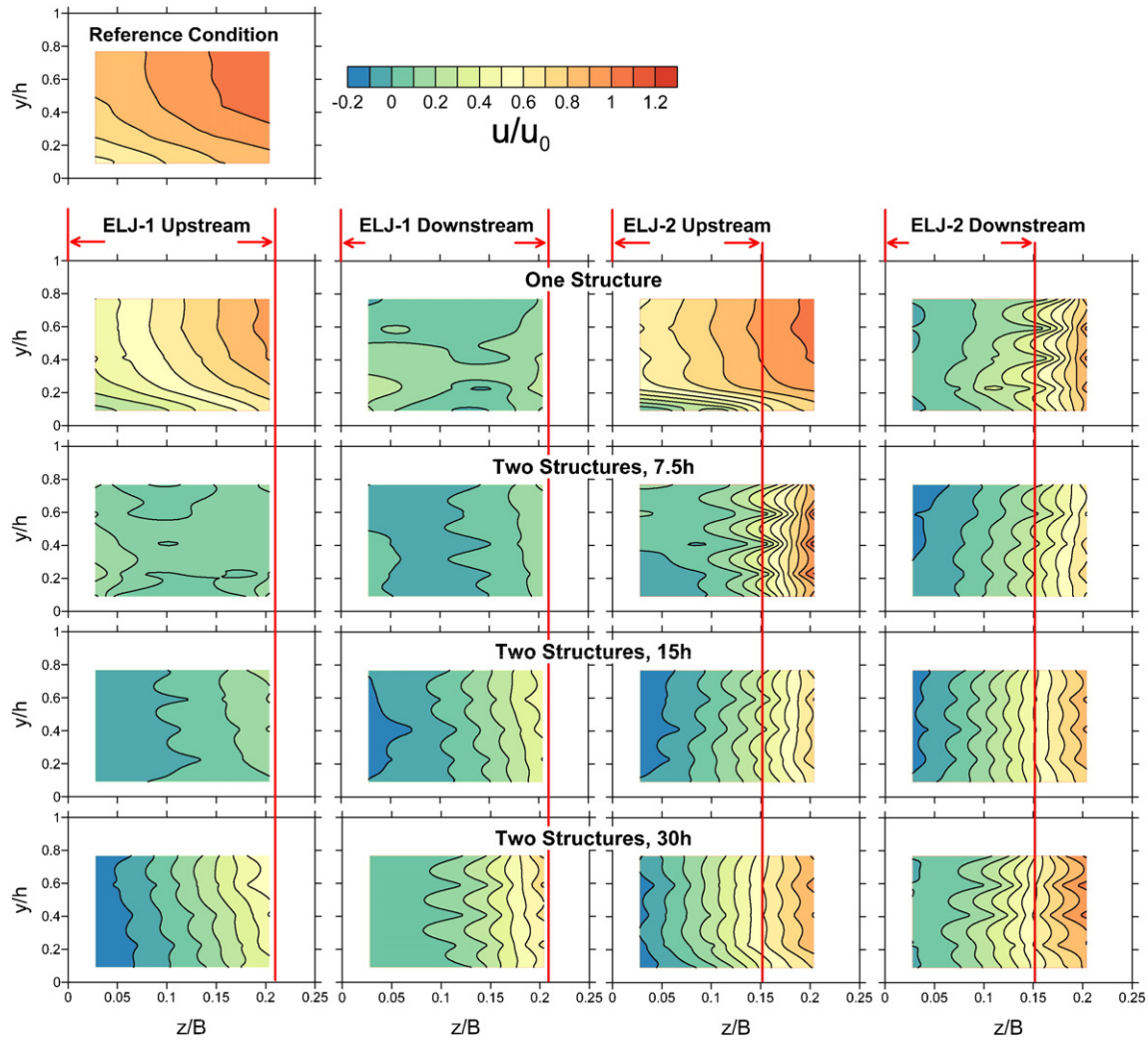


Fig. 10. Contour plots of normalized downstream flow velocity in the near-flow field for the reference condition (configuration 1), upstream and downstream of a single ELJ (configuration 2 for ELJ-1 on left and configuration 9 for ELJ-2 on right), and upstream and downstream of two ELJ structures at different spacing based on flow depth (configuration 3 for ELJ-1 on left and configuration 10 for ELJ-2 on right).

structures are not affected by the presence of the structures downstream, as F_D (Figs. 13 and 14) and C_D (Fig. 15) for the leading structure are similar to the single structure. Reduction in drag coefficient appears to be an artifact of the sheltering (wake) effects of an upstream structure. The measured drag forces on the ELJs are greatly reduced when upstream structures are present (Figs. 13 and 14), and this observation is accompanied by much lower incident flow velocities (Figs. 10, 11, and 12).

3.6. Momentum analysis

A primary objective of the current work was to measure the drag force acting on engineered log jams and to quantify the drag coefficients for these structures. In natural rivers, measurement of drag forces on ELJs or LW might be difficult or impossible (Hygelund and Manga, 2003; Shields and Alonso, 2012), yet knowledge of their drag coefficients would be very helpful for design purposes or the assessment of flow resistance. The existence of a measurable force on the ELJ means that the conservation of fluid momentum within a control volume should be applicable, provided the necessary data, and that this balance should be in agreement with the observations herein. A momentum balance is performed using the measured parameters for the single structure installations for ELJ-1 and ELJ-2 (Tables 1 and 3) to assess the

drag forces acting on the structures and to compare these results to the measured forces.

The analytical formulation is based on a finite control volume C.V. encompassing a longitudinal portion of the channel bounded by the upstream and downstream cross-sections where flow data are available. The steady state momentum equation governing fluid motion through this control volume can be expressed in integral form as

$$\iiint_{C.V.} \rho \vec{g} dV + \iint_{C.S.} \vec{n} \cdot (-p\mathbf{I} + \mathbf{T}) dA + \vec{F}_D = \iint_{C.S.} \rho \vec{V} (\vec{n} \cdot \vec{V}) dA \quad (9)$$

where C.S. is the control surface, dV is a fluid volume element within the C.V., \vec{V} is the velocity vector, p is pressure, \mathbf{I} is the unit tensor, \mathbf{T} is the shear stress tensor, \vec{F}_D is the drag force associated with the ELJ, A is flow area, and \vec{n} is the unit normal vector, which by definition is positive pointing outward from the C.V. (e.g., Chow, 1959). As flow is confined to a straight channel, it is sufficient to consider only the longitudinal components of Eq. (9),

$$\begin{aligned} \rho \iiint_{C.V.} g S dV + \iint_{C.S.} \vec{n} \cdot (-p\mathbf{I} + \mathbf{T}) dA - F_D \\ = -\rho \iint_{A_1} V_1^2 dA_1 + \rho \iint_{A_2} V_2^2 dA_2 \end{aligned} \quad (10)$$

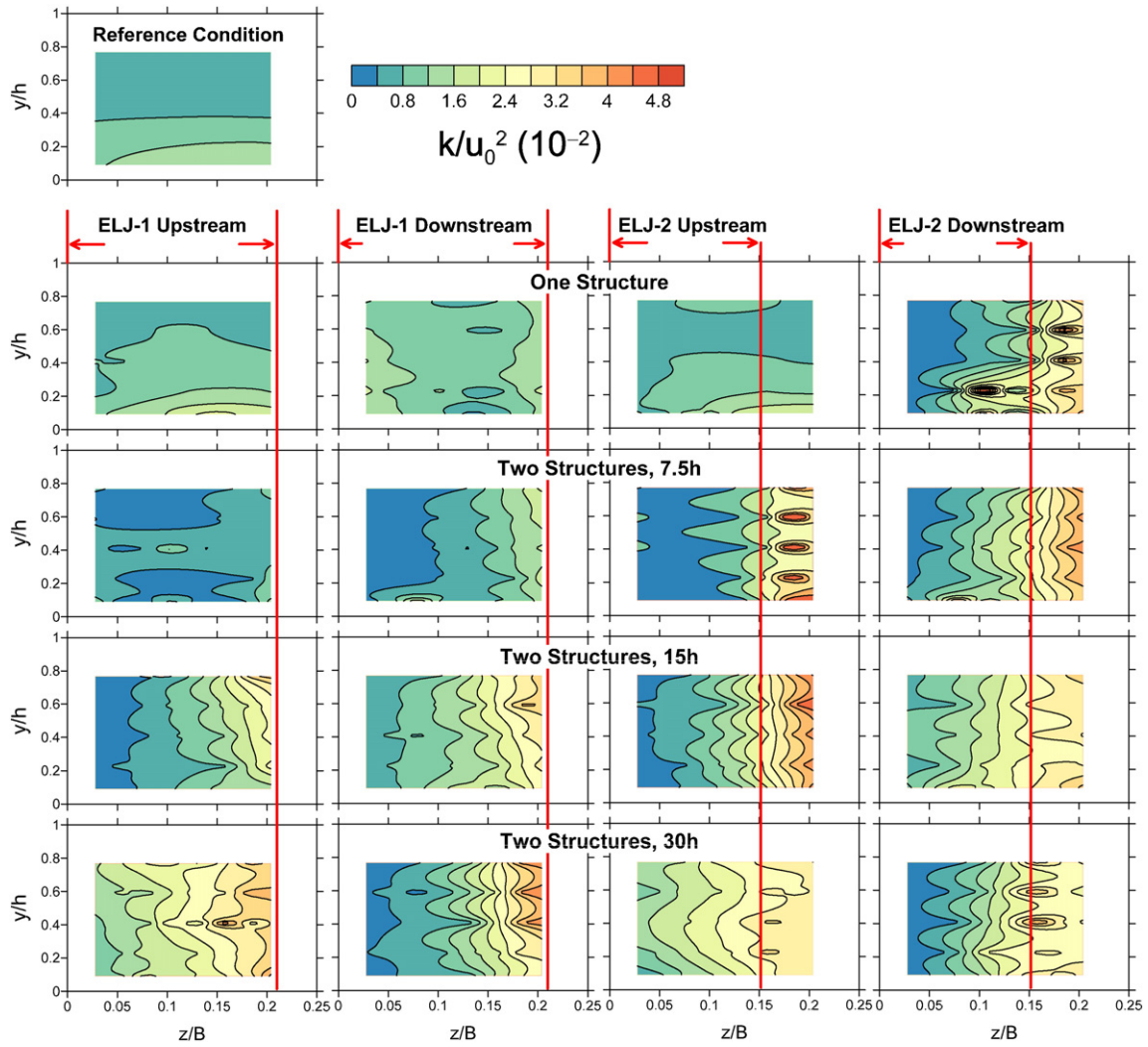


Fig. 11. Contour plots of normalized turbulent kinetic energy k in the near-flow field. Refer to Fig. 10 for additional details.

where ρ is assumed to be constant. Assuming further that pressures at the inflow and outflow cross-sections are hydrostatically distributed, writing in finite form yields

$$\gamma \nabla S + \sum_{B_1} \frac{1}{2} \gamma h_i^2 B_i - \sum_{B_2} \frac{1}{2} \gamma h_i^2 B_i - \bar{\tau}_b A_b - \bar{\tau}_w A_w - F_D = -\rho \sum_{A_1} V_j^2 A_j + \rho \sum_{A_2} V_j^2 A_j \quad (11)$$

where γ is the specific weight of water, h_i is the representative flow depth of interval i of the cross-section, B_i is the width of interval i , $\bar{\tau}_b$ and $\bar{\tau}_w$ are the spatially-averaged bed and wall shear stresses of the control volume, respectively, A_b and A_w are the bed and wet wall areas, respectively, V_j is the representative longitudinal velocity of cell j of the cross-section, and A_j is the area of cell j . Terms on the LHS of Eq. (11) are, respectively, forces of gravity G , upstream pressure P_1 , downstream pressure P_2 , bed shear stress, sidewall shear stress, and the drag force on the ELJ. Terms on the RHS are, respectively, fluxes of upstream M_1 and downstream momentum M_2 . The following assumptions are made: (i) $\bar{\tau}_b = \frac{1}{2} (0.23 \langle \tau_k \rangle_1 + 0.23 \langle \tau_k \rangle_2)$, using the above definition of boundary shear stress, where the subscripts denote the cross-section; (ii) $\bar{\tau}_w$ is determined using the formulation of sidewall shear stress for a uniform, smooth open channel suggested by Guo and Julien (2005); and (iii) total volume ∇ is calculated neglecting the subtraction of the small volume occupied by ELJs. In addition, four methods were used to evaluate the two terms on the RHS: (i) the velocities at all boundaries

were equal to the nearest velocity measurement; (ii) the region of interest was restricted only to the area where data were collected; (iii) the velocities along the wall, the bed, and the water surface were assumed

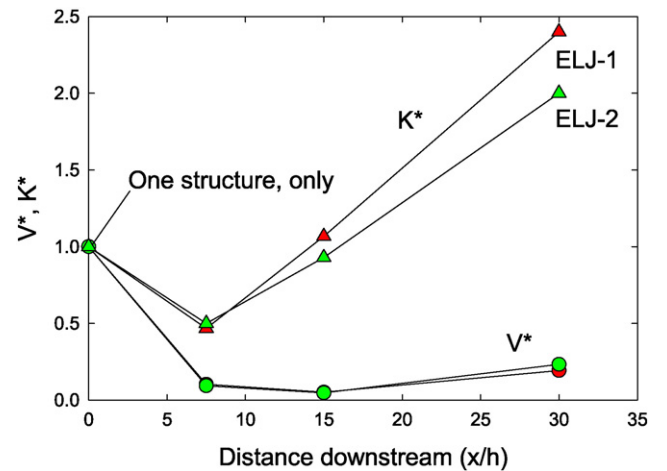


Fig. 12. Spatially averaged near-field downstream velocity V^* and turbulent kinetic energy K^* determined upstream of ELJ-1 (configuration 3) and ELJ-2 (configuration 10), and normalized by the values observed for a single structure (configuration 2 for ELJ-1 and 9 for ELJ-2), as a function of downstream distance from the upstream structure.

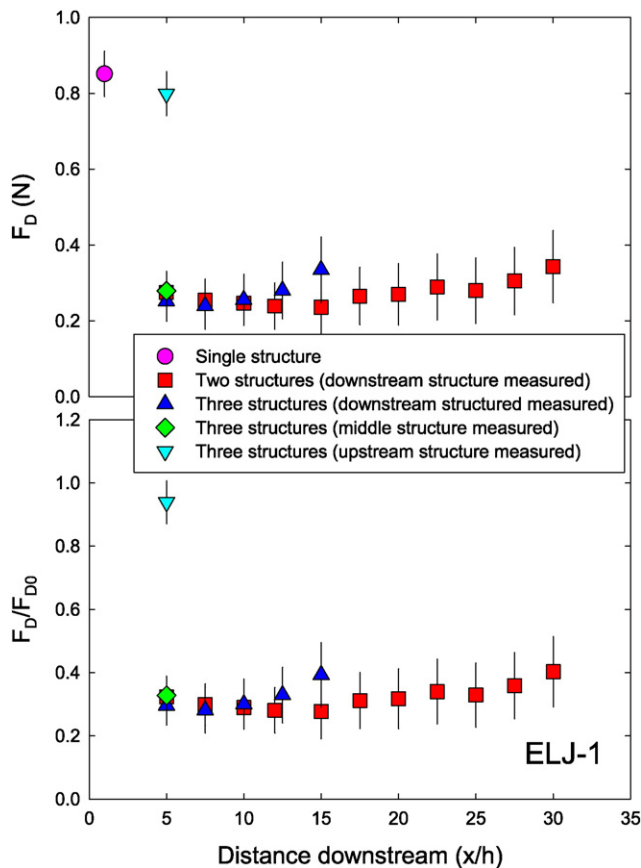


Fig. 13. Measured (upper) and normalized (lower) drag force acting on ELJ-1 for different configurations and spacing of structures. Error bars show the standard deviation of each measurement.

to be equal to 0.8, 0.9, and 1.01 times the nearest velocity measurement, respectively, as verified by actual measurements and by invoking flow continuity; and (iv) the velocities along the wall and the bed were assumed to be zero (a no-slip condition), and the velocity at the water surface was assumed to be equal to 1.01 times the nearest velocity measurement.

The results from the momentum analysis are summarized as follows: $F_D \approx -1.63$ to -1.48 N for ELJ-1, and $F_D \approx 1.71$ to 1.85 N for ELJ-2, depending on the averaging method employed. The calculated values of F_D clearly do not agree with the observations (Figs. 13 and 14), and in particular the negative values for ELJ-1 are unexpected. A sensitivity analysis for terms on the LHS of Eq. (11) was conducted to quantify the effects of measurement uncertainty on the calculated values of F_D . This analysis was accomplished by assigning experimental uncertainties to all parameters and by quantifying the range of calculated F_D on the basis of these uncertainties (this analysis included 10^6 calculations). These results show that P_1 and P_2 are extremely sensitive to these uncertainty ranges, suggesting that the pressure terms are most important when calculating the drag force by momentum analysis. Turcotte et al. (2015) used a simplified momentum balance to determine the drag force acting on a submerged cylinder. They noted that when the cylinder was relatively small in diameter, the difference in flow depth upstream and downstream of the cylinder was small or negligible. The derived drag forces in such experimental situations also would be small or negligible, which is consistent with the observations here. While the current results are inconclusive, this analysis does highlight the difficulty in applying, and the uncertainty in calculating, a momentum balance to quantify the drag force acting on LW in natural rivers and the need for high-quality data of sufficient spatial resolution.

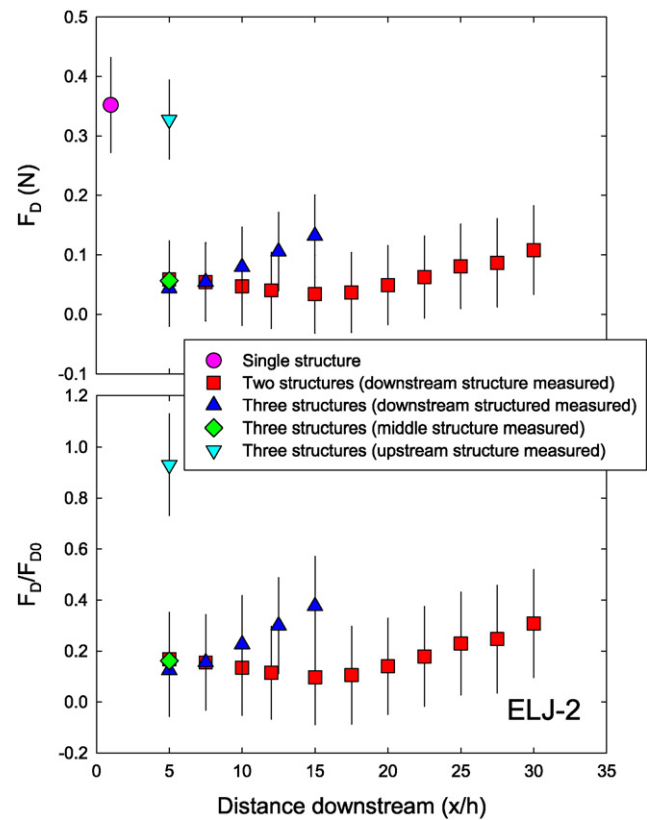


Fig. 14. Measured (upper) and normalized (lower) drag force acting on ELJ-2 for different configurations and spacing of structures. Error bars show the standard deviation of each measurement.

4. Discussion

The effects of engineered log jams on flow in an experimental channel are twofold. Near the structure, ELJs can significantly reduce flow velocity and bed shear stress in the near-bank regions and, in particular, in the areas downstream of the structure. An acceleration of flow is observed around the structure, accompanied by higher turbulence intensities and bed shear stresses near the structure in the main channel flow. On the basis of the conditions imposed, reduced near-bank flow velocities can extend to distances $>30h$ downstream. Yet ELJs have little effect on spatially-averaged flow upstream or downstream of the structure. These observations are consistent with previous findings showing that LW in rivers reduces velocities near the structure, produces a zone of stagnation downstream of the structure, and shifts the maximum velocity away from the structure and toward the main channel (Thorne and Furbish, 1995; Gippel et al., 1996; Daniels and Rhoads, 2003). The current paper further qualifies these hydraulic effects and their variations in space within an experimental channel.

Because of these hydraulic effects, ELJs can function very effectively as bank protection. When introduced, the energy in near-bank regions is reduced (see Figs. 10, 11, and 12), which may facilitate bank stability, sediment deposition, and nutrient sequestration (Abbe et al., 2003b; Brooks et al., 2004). The ELJs also can create scour holes around the perimeter of the structure where accelerated flow, elevated turbulence intensities, and higher bed shear stresses occur (see Fig. 9). These channel changes could increase geomorphic and hydraulic complexity as well as the amount of habitat available for a range of aquatic species (Gippel et al., 1996; Rhoads et al., 2003; Abbe et al., 2003b; Manners et al., 2007). Introducing ELJs to a disturbed stream has been shown to increase physical habitat diversity, including the development of zones of secondary flow that many fish species exploit as refugia or feeding zones (Shields et al., 2006; He et al., 2009). From these attributes, ELJs

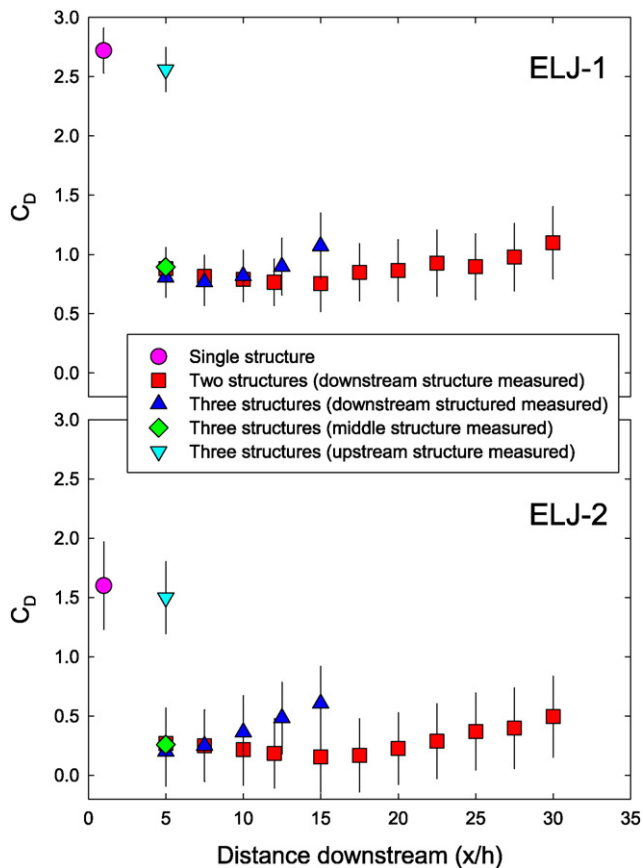


Fig. 15. Drag coefficients for different configurations of ELJ-1 (upper) and ELJ-2 (lower) structures. Error bars show the standard deviation of each calculation.

could fulfill the goals of stream restoration projects that aim to protect stream banks from hydraulic attack and to augment in-stream habitat for aquatic species.

This experimental study provides additional insight for design consideration. As noted by Shields and Alonso (2012), a wide range of C_D values has been reported for LW in rivers and engineered log jams (from 0.3 to 9). The reasons for this wide range include the effects of wood roughness, orientation, and relative submergence (Alonso, 2004), the complexity of the LW configurations (Manners et al., 2007), and potentially the methods used to derive C_D (Wallerstein et al., 2002; Turcotte et al., 2015). Based on the measurements obtained, and in light of previous work, C_D values for engineered log jams of the type employed here should be in the range of 1 to 3 using the spatially-averaged flow velocity of the channel as the characteristic velocity. These drag coefficients then can be used with numerical models to assess the morphodynamic responses of river channels to the introduction of ELJs and their impact on flow resistance. The drag associated with ELJ-1 is greater than ELJ-2, which explains the higher near-structure turbulence intensities and bed shear stresses. Such hydraulic signatures for ELJ-1 would likely increase the potential for greater scour depths and larger channel areas of influence as compared to ELJ-2. Both ELJ structures, however, still would afford significant bank protection downstream.

Effective ELJ designs rely upon careful consideration of the balance of forces acting on the structures. This force balance analysis is not trivial, and select examples include Shields et al. (2004), Abbe and Brooks (2011), and Shields and Alonso (2012). For practical purposes, Abbe and Brooks (2011) simplified this force balance approach for engineering applications, noting that the sum of the net horizontal force can be reduced to hydrostatic, buoyancy, and drag forces. This simplification appears to be consistent with the results presented here, most notably

that the observed drag forces for the ELJs are about an order of magnitude greater than the observed transverse forces. Since ELJs typically are ballasted by gravel and cobbles (D'Aoust and Millar, 2000; Brooks et al., 2006; Abbe and Brooks, 2011), the buoyancy force will be addressed. As such, the installation of piers into the banks and stream banks should focus on withstanding the drag forces of the design flow.

Limitations to the current study should be noted when considering ELJ design in natural streams. The prototype of the physical model, using a design discharge of $Q_{1.5}$, has a relatively low Froude number ($Fr \approx 0.12$), $w/h \approx 18$, a relatively shallow bed slope ($S \approx 0.0005$), and a very fine sand bed (Table 1). The magnitude of the river's morphodynamic response, and hence the efficacy of the ELJs, will be conditioned by these boundary conditions. The ELJ structures examined here, and the results observed, are based on the designs currently proposed by Brooks et al. (2006), which could change as additional information becomes available. Long-term monitoring of select installations continues, and some morphodynamic and ecologic responses in select rivers have been observed even five years after ELJ installation. Post-project assessment of ELJs is an important component to measure the resiliency of stream channel responses, especially given that the positive ecological effects may not be sustained over a period of years depending upon the integrity of the in-stream structures and adverse watershed-scale effects on ecosystems (Shields et al., 2005, 2007).

5. Conclusions

An experimental study was conducted to assess the effects of engineered log jams on the mean and turbulent flow in a fixed-bed, rectangular channel and to define the forces acting on these structures. The experiment employed Froude-number scaling principles to evaluate and compare two bank-attached deflector jams based on recommended designs, and devices to measure turbulent velocities near the structures and the drag and transverse forces acting on the structures in a wide range of configurations. The primary results are summarized as follows.

- The introduction of ELJs into a fixed-bed flow markedly affected regions near the structure, causing a slight backwater immediately upstream, flow acceleration around, and flow deceleration immediately downstream of the ELJs. A highly turbulent, vertically oriented shear layer was created near the structure whose transverse distance into the main flow appears to be similar in dimension to the ELJ penetration distance. Bed shear stresses also were elevated near this shear layer, and they were reduced in the near-bank regions downstream. These hydraulic effects were more pronounced in the presence of ELJ-1 as compared to ELJ-2, primarily because of differences in the size, shape, and orientation of the structures.
- Despite these localized perturbations, the introduction of a single ELJ had no effect on spatially-averaged flow just upstream and downstream of the structure.
- When two or three structures were deployed in tandem, the upstream structure created a relatively long wake region, in excess of 30 h , effectively shielding the downstream structure and the stream bank from the full brunt of the time-mean drag forces in the main channel flow. Qualitatively, this effect was similar for both ELJ types, although slight differences in turbulent kinetic energy were observed.
- Measured drag forces acting on the ELJs were about 10 times larger than the transverse forces. Drag coefficients using the spatially-averaged flow velocity from the reference condition were 2.72 ± 0.19 for ELJ-1 and 1.60 ± 0.37 for ELJ-2. Drag forces acting on the ELJs were markedly reduced when a structure was present upstream and shielded the downstream structures, and this also reduced drag coefficients. Application of a momentum balance to derive analytically the drag force acting on the ELJ based on collected hydraulic data proved inconclusive because of uncertainties in the experimental data required to calculate these relatively small forces.

These experimental results provide further insight into the design criteria necessary for the effective deployment of ELJs in rivers. First, ELJs provide significant bank protection via flow deceleration, exceeding distances of 30 h or more without any effect of spatially-averaged flow. Second, the drag coefficients reported here can be used to quantify the balance of forces acting on ELJs in field conditions as well as aid in the assessment of ELJs in river corridors using numerical models. The results presented herein, however, are conditioned by the characteristics of the prototype selected and the ELJ designs employed.

Acknowledgments

We thank Kevin Cullinan, Tom Gruenauer, and Tim Martz for technical assistance during the construction of the flume; Sol Brich for providing much of the background information on the Big Sioux River; and Andrew Brooks for information on engineered log jams. This research was financially supported by the City of Sioux Falls, SD, and the USDA-ARS (Specific Research Agreement No. 58-6408-9-346). We thank the four anonymous referees and Richard Marston who provided many helpful suggestions on ways to improve the manuscript.

References

- Abbe, T., Brooks, A., 2011. Geomorphic, engineering, and ecological considerations when using wood in river restoration. In: Simon, A., Bennett, S.J., Castro, J.M. (Eds.), *Stream Restoration in Dynamic Fluvial Systems: Scientific Approaches, Analyses, and Tools*. Geophysical Monograph Series 194. American Geophysical Union, Washington, DC, pp. 419–451.
- Abbe, T.B., Montgomery, D.R., 1996. Large woody debris jams, channel hydraulics and habitat formation in large rivers. *Regul. Rivers Res. Manag.* 12, 201–221.
- Abbe, T.B., Brooks, A.P., Montgomery, D.R., 2003a. Wood in river rehabilitation and management. In: Gregory, S.V., Boyer, K.L., Gurnell, A.M. (Eds.), *The Ecology and Management of Wood in World Rivers*. American Fisheries Society Symposium 37. American Fisheries Society, Bethesda, MD, pp. 367–389.
- Abbe, T., Pess, G., Montgomery, D.R., Fetherston, K., 2003b. Integrating engineered log jam technology into reach-scale river restoration. In: Montgomery, D.R., Bolton, S., Booth, D.B., Wall, L. (Eds.), *Restoration of Puget Sound Rivers*. University of Washington Press, Seattle and London, pp. 443–482.
- Alonso, C.V., 2004. Transport mechanics of stream-borne logs. In: Bennett, S.J., Simon, A. (Eds.), *Riparian Vegetation and Fluvial Geomorphology*. Water Sci. Appl. vol. 8. American Geophysical Union, Washington, DC, pp. 59–69.
- Bennett, S.J., Bridge, J.S., Best, J.L., 1998. Fluid and sediment dynamics of upper-stage plane beds. *J. Geophys. Res.* 103 (C1), 1239–1274.
- Bennett, S.J., Wu, W., Alonso, C.V., Wang, S.S.Y., 2008. Modeling fluvial response to in-stream woody vegetation: implications for stream corridor restoration. *Earth Surf. Process. Landf.* 33, 890–909.
- Biron, P.M., Robson, C., Lapointe, M.F., Gaskin, S.J., 2004. Comparing different methods of bed shear stress in simple and complex flow fields. *Earth Surf. Process. Landf.* 29, 1403–1415.
- Bisson, P.A., Bilby, R.E., Bryant, M.D., Dolloff, C.A., Grette, G.B., House, R.A., Murphy, M.L., Koski, K.V., Sedell, J.R., 1987. Large woody debris in forested streams in the Pacific Northwest: past, present, and future. In: Salo, E.O., Cundy, T.W. (Eds.), *Streamside Management: Forestry and Fishery Interactions*. College of Forest Resources, Contribution 57. University of Washington, Seattle, pp. 143–190.
- Brooks, A.P., Gehrke, P.C., Jansen, J.D., Abbe, T.B., 2004. Experimental reintroduction of woody debris on the Williams River, NSW: geomorphic and ecological responses. *River Res. Appl.* 20, 513–536.
- Brooks, A., Abbe, T., Cohen, T., Marsh, N., Mika, S., Boulton, A., Broderick, T., Borg, D., Rutherford, I., 2006. Design Guideline for the Reintroduction of Wood into Australian Streams. Land & Water Australia, Canberra (85 pp.).
- Buffington, J.M., Lisle, T.E., Woodsmith, R.D., Hilton, S., 2002. Controls on the size and occurrence of pools in coarse-grained forest rivers. *River Res. Appl.* 18, 507–531.
- Cai, D., 2014. Effects of Engineered Log Jams on Mean and Turbulent Flow in an Open Channel (M.S. thesis). Department of Geography, University at Buffalo (51 pp.).
- Chow, V.T., 1959. *Open-channel Hydraulics*. The Blackburn Press, Caldwell (680 pp.).
- Collins, B.D., Montgomery, D.R., Fetherston, K., Abbe, T.B., 2012. The floodplain large-wood cycle hypothesis: a mechanism for the physical and biotic structuring of temperate forested alluvial valleys in the North Pacific coastal ecoregion. *Geomorphology* 139–140, 460–470.
- D'Aoust, S.G., Millar, R.G., 2000. Stability of ballasted woody debris habitat structures. *J. Hydraul. Eng.* 126, 810–817.
- Daniels, M.D., Rhoads, B.L., 2003. Influence of a large woody debris obstruction on three-dimensional flow structure in a meander bend. *Geomorphology* 51, 159–173.
- Flores, L., Larranaga, A., Diez, J., Elosegi, A., 2011. Experimental wood addition in streams: effects on organic matter storage and breakdown. *Freshw. Biol.* 56, 2156–2167.
- Gallisdorfer, M.S., Bennett, S.J., Atkinson, J.F., Ghaneeizad, S.M., Brooks, A.P., Simon, A., Langendoen, E.J., 2014. Physical-scale model designs for engineered log jams in rivers. *J. Hydro Environ. Res.* 8, 115–128.
- Gippel, C.J., O'Neill, I.C., Finlayson, B.J., Schnatz, I., 1996. Hydraulic guidelines for the re-introduction and management of large woody debris in lowland rivers. *Regul. Rivers Res. Manag.* 12, 223–236.
- Goring, D.G., Nikora, V.I., 2002. Despiking acoustic Doppler velocimeter data. *J. Hydraul. Eng.* 128, 117–126.
- Guo, J., Julien, P.Y., 2005. Shear stress in smooth rectangular open-channel flows. *J. Hydraul. Eng.* 131, 30–37.
- He, Z., Wu, W., Shields Jr., F.D., 2009. Numerical analysis of effects of large wood structures on channel morphology and fish habitat suitability in a Southern US sandy creek. *Ecohydrology* 2, 370–380.
- Huthnance, J.M., Humphery, J.D., Knight, P.J., Chatwin, P.G., Thomsen, L., White, M., 2002. Near-bed turbulence measurements, stress estimates and sediment mobility at the continental shelf edge. *Prog. Oceanogr.* 52, 171–194.
- Hygelund, B., Manga, M., 2003. Field measurements of drag coefficients for model large woody debris. *Geomorphology* 51, 175–185.
- Kim, S.C., Friedrichs, C.T., Maa, J.P.Y., Wright, L.D., 2000. Estimating bottom stress in tidal boundary layer from acoustic Doppler velocimeter data. *J. Hydraul. Eng.* 126, 399–406.
- Lane, S.N., Biron, P.M., Bradbrook, K.F., Butler, J.B., Chandler, J.H., Crowell, M.D., McLelland, S.J., Richards, K.S., Roy, A.G., 1998. Three-dimensional measurement of river channel flow processes using acoustic Doppler velocimetry. *Earth Surf. Process. Landf.* 23, 1247–1267.
- Lautz, L.K., Siegel, D.I., Bauer, R.L., 2006. Impact of debris dams on hyporheic interaction along a semi-arid stream. *Hydrol. Process.* 20, 183–196.
- Lester, R.E., Boulton, A.J., 2008. Rehabilitating agricultural streams in Australia with wood: a review. *Environ. Manag.* 42, 310–326.
- Manners, R.B., Doyle, M.W., Small, M.J., 2007. Structure and hydraulics of natural woody debris jams. *Water Resour. Res.* 43, W06432. <http://dx.doi.org/10.1029/2006WR004910>.
- Montgomery, D.R., Buffington, J.M., Smith, R., Schmidt, K., Pess, G., 1995. Pool spacing in forest channels. *Water Resour. Res.* 31, 1097–1105.
- Nezu, I., Nakagawa, H., 1993. *Turbulence in Open-Channel Flows*. Balkema, Rotterdam (286 pp.).
- Rhoads, B.L., Schwartz, J.S., Porter, S., 2003. Stream geomorphology, bank vegetation, and three-dimensional habitat hydraulics for fish in midwestern agricultural streams. *Water Resour. Res.* 39, 1218. <http://dx.doi.org/10.1029/2003WR002294>.
- Shields Jr., F.D., Alonso, C.V., 2012. Assessment of flow forces on large wood in rivers. *Water Resour. Res.* 48, W04516. <http://dx.doi.org/10.1029/2011WR011547>.
- Shields Jr., F.D., Morin, N., Cooper, C.M., 2004. Large woody debris structures for sand bed channels. *J. Hydraul. Eng.* 130, 208–217.
- Shields Jr., F.D., Knight, S.S., Cooper, C.M., 2005. Stream ecosystem restoration: is watershed-scale treatment effective without instream habitat rehabilitation? *Ecol. Restor.* 23, 103–109.
- Shields Jr., F.D., Knight, S.S., Stoffeth, J.M., 2006. Large wood addition for aquatic habitat rehabilitation in an incised sand-bed stream, Little Topashaw Creek, Mississippi. *River Res. Appl.* 22, 803–817.
- Shields Jr., F.D., Knight, S.S., Copper, C.M., 2007. Can warmwater streams be rehabilitated using watershed-scale standard erosion control measures alone? *Environ. Manag.* 40, 62–79.
- Soulsby, R.L., 1983. The bottom boundary-layer in shelf seas. In: Johns, B. (Ed.), *Physical Oceanography of Coastal and Shelf Areas*. Elsevier, Amsterdam, pp. 189–266.
- South Dakota Department of Environment and Natural Resources, 2014. The 2014 South Dakota Integrated Report for Surface Water Quality Assessment. <http://denr.sd.gov/documents.aspx> (accessed June 10, 2015).
- Sukhodolov, A., Thiele, M., Bungartz, H., 1998. Turbulence structure in a river reach with sand bed. *Water Resour. Res.* 34, 1317–1334.
- Svoboda, C.D., Russell, K., 2011. Flume analysis of engineered large wood structures for scour development and habitat. World Environmental and Water Resources Congress 2011 Bearing Knowledge for Sustainability. American Society of Civil Engineers, pp. 2572–2581.
- Thorne, S.D., Furbish, D.J., 1995. Influences of course bank roughness on flow within a sharply curved river bend. *Geomorphology* 12, 241–257.
- Turcotte, B., Millar, R.G., Hassan, M.A., 2015. Drag forces on large cylinders. *River Res. Appl.* <http://dx.doi.org/10.1002/rra.2868>.
- Wahl, T.L., 2000. Analyzing ADV data using WinADV. Proc., Joint Conf. on Water Resources Engineering and Water Resources Planning and Management. ASCE, Reston, Va.
- Wallerstein, N.P., Thorne, C.R., 2004. Influence of large woody debris on morphological evolution of incised, sand-bed channels. *Geomorphology* 57, 53–73.
- Wallerstein, N.P., Alonso, C.V., Bennett, S.J., Thorne, C.R., 2001. Distorted Froude-scaled flume analysis of large woody debris. *Earth Surf. Process. Landf.* 26, 1265–1283.
- Wallerstein, N.P., Alonso, C.V., Bennett, S.J., Thorne, C.R., 2002. Surface wave forces acting on submerged logs. *J. Hydraul. Eng.* 128, 349–353.
- Williams, J.J., Rose, C.P., Thorne, P.D., O'Connor, B.A., Humphery, J.D., Hardcastle, P.J., Moores, S.P., Cooke, J.A., Wilson, D.J., 1999. Field observations and predictions of bed shear stresses and vertical suspended sediment concentration profiles in wave-current conditions. *Cont. Shelf Res.* 19, 507–536.